IEEE Access
The journal for rapid open access publishing

IEEE Xplore Digital Library
http://ieeexplore.ieee.org/Xplore

# TV Regularized Low-rank Framework for Localizing Premature Ventricular Contraction Origin

LIN FANG[1], QI ZHUANG[2], WEI MAO[3], YUNMEI CHEN[4], and HUAFENG LIU [1]

***Abstract*—Premature ventricular contraction (PVC) can cause great harm to human health. Both invasive and non-invasive techniques for detecting electrical activity of PVC or locating ectopic pacemakers are used in clinical diagnosis. Among them, the electrocardiographic imaging is a popular method for non-invasive reconstruction of cardiac electrophysiology through body-surface potential. In this paper, we propose a novel framework based on low-rank and sparse decomposition (LSD) + total variation (TV) to solve the ill-posedness of the spatiotemporal ECG-inverse problem to reconstruct the cardiac electrical activity of PVC. The proposed framework considers the spatiotemporal distribution of multi-frame cardiac potential as a whole. TV is used to filter out relatively smooth candidates from countless inverse solutions. In addition, LSD utilizes the low-rank characteristic of the potential background and the sparseness of the potential outliers to avoid the loss of potential details and improve the accuracy of potential reconstruction. This improves the quality of electrical activity retrieval and the accuracy of locating the PVC origin. Simulation experiments of ventricular pacing reconstruction and diagnostic experiments of real PVC patients prove that the proposed framework is superior to the conventional quadratic methods (Tikhonov-0, Tikhonov-2) and the non-quadratic method TV.**

***Index Terms*—Inverse problem of electrocardiography, total variation, low-rank, sparsity.**

## I. Introduction

THE ever-increasing medical technology provides extensive means for the diagnosis of premature ventricular contraction (PVC), which is associated with increased risk of sudden cardiac death and can cause secondary cardiomyopathy. Accurate localization of PVC is essential for a successful catheter ablation procedure. In clinical electrophysiology, two invasive catheter mapping systems (CARTO, Ensite) can offer a 3D reconstruction of the heart chamber while being examined together with imaging of mapping and ablation catheters [1], [2]. However, for some cases they pose certain limitations regarding the location of arrhythmia and long-term monitoring.

Consequently, a variety of non-invasive ill-posed inverse techniques has been proposed to provide more detailed information on the spatial and temporal distribution of cardiac electrophysiological activity to accurately localize the PVC origin. Most of the efforts along this line are based on the measurements obtained from body-surface potential mapping (BSPM) [3], which record the potentials through a large number of electrodes (32-256) placed on the body surface to compensate for the missing information of the standard 12-lead electrocardiography (ECG). Broadly speaking, there are two large groups of methods based on the solution of the activation sequence [4], [5] and the electric potential on the heart surface (epicardial or/and endocardial [6], and transmurally [7]).

The imaging of cardiac activation time reconstitutes the electrical activation sequence in the heart, that is, the arrival time of the action potential depolarization phase, which has important clinical significance [5], [8]. The heart-surface activation time [9] itself can directly be the solution to the inverse problem of ECG by solving linear or nonlinear ill-conditioned inverse problems. Alternatively, the heart activation time can also be derived indirectly from the cardiac potential [6]. Further, three-dimensional activation imaging was proposed by He's group [10], [11] to extend the mapping result of the cardiac surface to the three-dimensional myocardial volume, thereby achieving electrical tomography imaging of cardiac activation. However, most methods of cardiac activation imaging rely on explicit physiological assumptions of the cardiac activation process (e.g., conduction velocity or template functions for transmembrane potentials).

Alternatively, the other form of electrophysiological imaging is to estimate the distribution of electrical potential of a closed heart surface or transmural myocardial wall from the body-surface potential mapping. The solutions of the electrical potential have more general physiological significance. The potential amplitude itself is a marker for identifying infarction or slow-conduction zones [12], [13]. On the other hand, some clinically interesting parameters can also be derived from potentials, such as electrical activation time, which is widely used in focusing the origin of an arrhythmia. In this study, we concentrated on the localization of the PVC origin by reconstructing the electrical potentials on a closed heart surface (endo- and epicardial).

For most electrophysiological imaging purposes, the following materials are required: data of the multi-lead [14] body-surface potentials and a heart torso geometry model, which can be created from computerized tomographic (CT) scanning or magnetic resonance imaging (MRI). From these, a linear or non-linear forward system that relates the cardiac electrophysiology to the body-surface potential can be derived by means of the boundary element method (BEM) [15], [16] or the finite-element method (FEM) [17]. Finally, to solve the ill-posed inverse problem with any existing successful methods, a formulation must be established to select the best solution with the available prior knowledge. Regarding the prior knowledge, a significant level of activity has been performed, which is generally based on quadratic or non-quadratic characteristics of the spatiotemporal inverse electrical information.

Various spatial-constrained methods have been developed to reduce the ill-posedness of the electrophysiological inverse problem. For instance, Tikhonov approaches, which drew the first uniformly accepted methods, are based on constraining

Digital Object Identifier: 10.1109/ACCESS.2019.2899696



IEEE

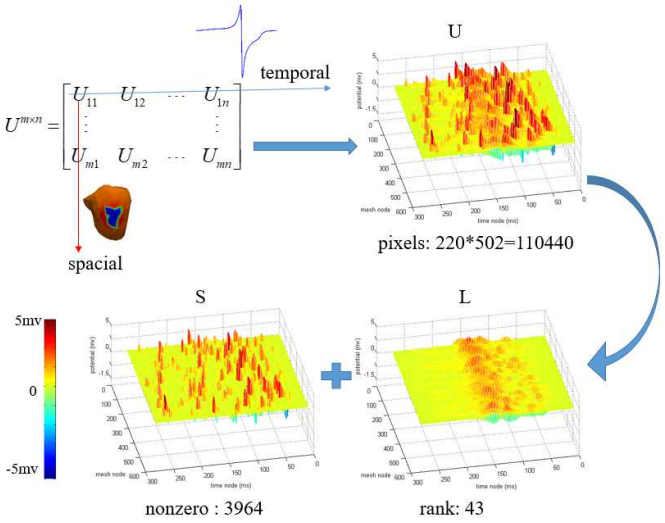


Fig. 1: Process of low-rank and sparse decomposition of spatio-temporal EEP. $U^{\mathrm{m}\times n}$ is the EEP spatiotemporal distribution of $m$ mesh nodes and $n$ time nodes. $L$ indicates the low-rank background and $S$ corresponds to the sparse foreground.

the L2 norm of the "energy" or a nth-order derivative (e.g., the gradient or Laplacian estimate) of the solution [18]–[21]. Tikhonov regularization tries to find a trade-off between a good fit to the body surface data and a priori information about the cardiac data by a balance parameter, which can be determined by L-curve [22], or zero crossing methods [23]. Other noteworthy efforts in particular include truncated singular-value decomposition (TSVD) [24]–[26], truncated total least squares (TTLS) [27], least-squares QR (LSQR) [28], level-set [29] and Bayesian estimation [30]. However, among them, the L2-norm constraints inherently provide smoothed solutions, thus compromising accuracy required for capturing the lesion (e.g., localizing an arrhythmic focus) [6]. More recently, to overcome the drawbacks of L2-norm methods, several algorithms based on L1-norm minimization have been proposed to tackle the cardiac potential reconstruction problem. The most typical application is known as total variation (TV), which constrains the L1-norm of the potential gradient, thus obtaining less blurring and edge-preserving inverse solutions. Ghosh and Rudy [6] performed the TV-based scheme in epicardial potential reconstruction and location of the epicardial pacing sites, where the L1-norm method outperformed the quadratic methods in accuracy. Later, some TV extension methods such as [31] were produced. For the reconstruction of dynamic electrical potentials, those innovative temporal models have been successfully applied. Typically, Oster and Rudy applied the Twomey regularization [32] to balance residuals and error estimates, in which the temporal regularization was used after the spatial regularization step to enhance the temporal correlation of the solution. Other well-known spatiotemporal methods include Kalman filters [33] and the isotropy method [34].

Most of the previous methods use spatial or temporal smoothness/sparseness to select an optimal solution from the non-unique candidates. There may be certain limitations because cardiac electrophysiological dynamics behave differently at different periods of a cardiac cycle, which may not coincide with smooth or sparse characteristics at any time, especially in pathological myocardial tissue. To image the potential at any position on the heart surface during any period, in this paper, a novel method based on low-rank and sparse decomposition + TV (LSDTV) has been proposed to reconstruct dynamic endo- and epicardial potential (EEP). The spatiotemporal dynamics of the EEP consist of an appropriate combination of a low-rank background and a sparse foreground, which more generally conform to the spatiotemporal distribution of the EEP over any period of cardiac pacing rhythm. Based on this assumption, the spatial smoothness and the temporal correlation of the EEP are guaranteed by the low-rank and TV constraints on the potential background, while the potential spikes are retained by the sparse foreground. Actually, low-rank and sparse techniques have been successfully applied in dynamic MRI reconstruction [35], reconstruction and segmentation of positron emission tomography (PET) [36], spectral CT reconstruction [37], and many other areas of image or signal processing [38], [39].

The innovation of this method includes: 1) Low-rank constraint can take advantage of the spatiotemporal correlation of EEP dynamics, combined with a sparse constraint to provide sparse potential spikes information. 2) After the sparse potential spikes are separated, the TV regularization can enhance the local smooth structure of the EEP background, thereby promoting the filtering of Gaussian noise. To verify the effectiveness of the proposed LSDTV approach, experiments on simulated ventricular pacing data and real PVC data have been performed.

## II. Method

### A. Dynamic EEP-to-BSP model

In this part, we modeled the forward relationship between the heart-surface potential to the body-surface potential. The heart model in this study is an "uncapped" ventricular surface (epicardium and endocardium) model [34]. The ion flux of cardiomyocytes results in the variation of heart-surface potentials, projecting time-varying electrical signals onto the body surface through a quasi-static electromagnetic filed. Assuming that no other active electrical source exists between the heart and body surfaces, the cardiac electric field in the region bounded between the heart and body surfaces can be formulated by the standard Laplace equation [34]:

$$\sigma \nabla^2 \varphi\left(r\right) = 0 \tag{1}$$

where $\sigma$ is the torso conductivity scalar. $\varphi\left(r\right)$ stands for the potentials boundaried between the heart and body surfaces, generated by cardiac electrophysiological activity.

In terms of boundary conditions, there is no conductive medium outside the body surface. Therefore, the derivative of the body-surface potential in the normal direction is 0. In addition, the body-surface potential is a known amount that can be measured by placing the electrodes on the body surface. Therefore, the boundary conditions can be expressed as

$$\frac{\partial \varphi(r)}{\partial n} = 0 \quad on \;\; S_b \tag{2}$$

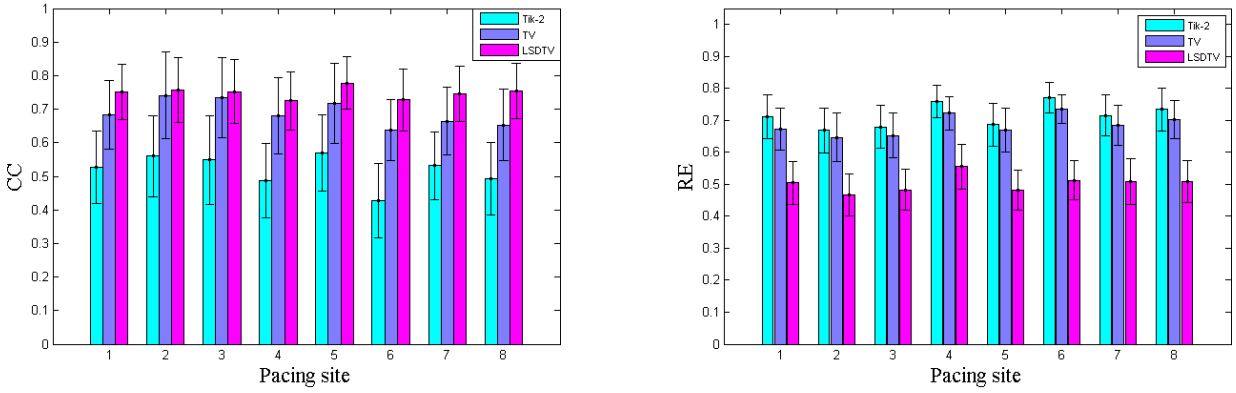


(a) (b)

Fig. 2: Accuracy of (a) CC and (b) RE on 8 cases of ventricular pacing statistical analysis. The color histograms represent the CC/RE average of all frames over the pacing rhythm. Error bars show the standard deviation of the results. The pacing sites in 8 different locations are: LV-anterior, LV-apex, LV-lateral-endo, LV-lateral-epi, LV-lateral, ventricular septum, RV-anterior, and RV-posterior.

$$\varphi(r) = \phi(r) \quad on \;\; S_b \tag{3}$$

$$\varphi(r) = u(r) \quad on \;\; S_h \tag{4}$$

where $S_b$ indicates the body surface and $S_h$ indicates the heart surface (epi and endo). $n$ represents the normal direction outward of the body surface $S_b$. $\phi(r)$ is the potential on $S_b$ at coordinate $r$. $u(r)$ indicates the extracellular potential on the heart surface $S_h$.

With the boundary conditions eq. (2)-(4), the Laplace equation eq. (1) can be solved by BEM [16]. Then, the forward relationship between the EEP and the BSP can be modeled as a linear transformation equation:

$$\boldsymbol{\phi} = Hu \tag{5}$$

$$\boldsymbol{\phi} \in R^{p\times 1} \quad u \in R^{m\times 1} \quad H \in R^{p\times m}$$

where $\boldsymbol{\phi}$ is a p-dimensional column vector representing potentials measured by p-lead electrodes on the body surface. $u$ is a column vector of the m-dimensional cardiac potentials. $H$ is a time-invariant transfer matrix specific to the heart-torso geometric model.

To consider a time sequence of heart-surface potentials: $U = [u_1, u_2, \cdots, u_i, \cdots, u_n]$, $U \in R^{m\times n}$, where $u_i$ is the $i$-th frame of the heart-surface potentials of $m$ mesh nodes, as a column in $U$, and the corresponding dynamic mapping of the body-surface potential matrix: $\Phi = [\boldsymbol{\phi}_1 \cdots, \boldsymbol{\phi}_i, \cdots \boldsymbol{\phi}_n]$, $\Phi \in R^{p\times n}$, where $\boldsymbol{\phi}_i$ represents the $i$-th frame of body-surface potentials of $p$-lead electrodes. The EEP-to-BSP forward model of the single-frame ECG can be extended to the multiple-frame form as:

$$\Phi = HU \tag{6}$$

### *B. LSDTV Framework*

A dynamic EEP reconstruction framework is introduced in detail. The spatiotemporal EEP matrix $U$ can be 3D-scaled as shown in Fig. 1. Then, it can be decomposed into a low-rank background $L$ (the relatively flat ingredient of EEP) and a sparse foreground $S$ (the non-zero element is sparse: red color represents the positive potential peak and blue color represents the negative potential valley, as shown in Fig. 1) as $U = L + S$. With this definition, the objective target of the inverse problem can be expressed as three processes: the fidelity term, TV penalty, and low-rank and sparse decomposition.

**Fidelity constrain:** With EEP-to-BSP definition, to ensure that the estimated cardiac potential data is in accordance with the actual body surface measurement data, the reconstructed EEP matrix $U$ should satisfy the following fidelity terms:

$$\min \; \|HU - \Phi\|_F^2 \tag{7}$$

where the Frobenius norm $\|A\|_F$ is defined for any matrix $A(m \times n)$ as $\|A\|_F = \sqrt{\sum_{i=1}^{m}\sum_{j=1}^{n} |A_{ij}|^2}$.

**TV constrain:** The TV constraint is used to force the smoothing of the potential background, thereby filtering out the noise disturbance. The TV penalty term can be formulated as:

$$TV(L) = \|\nabla L\|_1 = \sum\nolimits_{i=1}^{n} \sum\nolimits_{j=1}^{M} \left|\nabla f^j L_i\right| = \|DL\|_1 \tag{8}$$

$$s.t. \quad D = \begin{bmatrix} \nabla f^1 \\ \vdots \\ \nabla f^j \\ \vdots \\ \nabla f^M \end{bmatrix}$$

where a gradient summation is performed over the triangular discretized myocardial surface by $M$ Gaussian quadrature points, during a time range of $n$ time nodes. Based on the spatial gradient of the shape function, a gradient at each Gaussian point is approximated by its linear combination of adjacent nodes in the discrete field, where $f^j$ (with the dimension of $3 \times M$) is the shape function of the $j$-th mesh

node. $L_i$ is the $i$-th column of $L$. $D \in R^{3M\times M}$ is the dispersed gradient operator [40] composed by the gradient of the shape function of the whole $m$ mesh nodes. $\|A\|_1 = \sum_{ij}|A_{ij}|$ is the L1 norm of any matrix $A$ by treating the matrix $A(m\times n)$ as a long vector in $R^{m\cdot n}$.

**Low-rank and sparse decomposition:** While the TV smoothing constraint makes the potentials relatively flat, to avoid loss of potential details, these must be separated from the background by appropriate means. According to the composition of the potential foreground, as shown in Fig. 1, the potential detail matrix $S$ should be sparse. In this study, low-rank and sparse decomposition, namely Robust Principal Component Analysis (RPCA [41]), was used to separate EEP details from the potential background:

$$\min\ \|L\|_* + \|S\|_1 \quad s.t.\ U = L + S \tag{9}$$

where $\|L\|_*$ is the nuclear norm of the matrix $L$, that is, the sum of singular values of $L$ and is the convex relaxation of low-rank penalty $rank(L)$. In addition, the L1-norm item $\|S\|_1$ is the convex approximation of the real sparse constraint $\|S\|_0$, where the L0 norm $\|S\|_0$ represents the number of non-zero elements in the matrix $S$.

**Complete optimization objective:** Finally, some parameters are used to balance the fidelity constraint (eq. (7)), the TV constraint (eq. (8)), and the low-rank sparse decomposition terms (eq. (9)). Then, the optimization objective is:

$$\begin{aligned}\min\ \|L\|_* + \lambda\|S\|_1 + \gamma\|DX\|_1 + \frac{\mu}{2}\|HU-\Phi\|_F^2 \\ s.t.\ U = L + S,\ \ L = X\end{aligned} \tag{10}$$

where $\lambda$, $\gamma$, $\mu$ are balance parameters.

### C. Optimization method

In this study, the augmented Lagrangian function [41] was used to transform the constrained optimization problem shown in eq. (10) into the unconstrained minimization target:

$$\begin{aligned}\mathcal{L}(L,S,U,X) = \|L\|_* + \lambda\|S\|_1 - \langle Z, U-(L+S)\rangle \\ +\frac{\beta}{2}\|U-(L+S)\|_F^2 + \gamma\|DX\|_1 - \langle Z_L, L-X\rangle \\ +\frac{\beta_L}{2}\|L-X\|_F^2 + \frac{\mu}{2}\|HU-\Phi\|_F^2\end{aligned} \tag{11}$$

where $\beta$, $\beta_L$ are additional weighting factors. $Z$ and $Z_L$ are Lagrangian multipliers. It is difficult to solve all the unknown matrices $L$, $S$, $U$ directly. In this study, Alternating Direction Method of Multipliers (ADMM [42]) was used to decompose the augmented Lagrangian function (eq. (11)) into three subproblems, and then solve each subproblem by alternately updating them in successive iterations.

*1) L,S subproblem:* By combining the terms related to $L$ from the augmented Lagrangian function (eq. (11)) and scaling the dual variable [42], the $L$ subproblem can be formulated as:

$$\min\ \|L\|_* + \frac{\beta}{2}\|L-(U-S+Z/\beta)\|_F^2 + \frac{\beta_L}{2}\|L-(X+Z_L/\beta_L)\|_F^2 \tag{12}$$

Combining the two Frobenius-norm terms in eq. (12) to get the final form of the $L$ subproblem:

$$\min\ \|L\|_* + \frac{\beta+\beta_L}{2}\left\|L - \frac{\beta(U-S+Z/\beta)+\beta_L(X+Z_L/\beta_L)}{\beta+\beta_L}\right\|_F^2 \tag{13}$$

Previous work has proposed that the minimization problem of the nuclear norm as eq. (13) can be solved directly with singular value thresholding (SVT) [41]. The solution of the $L$ subproblem can be formulated by the following equation and subjection.

$$\begin{aligned}L = U_{Y_L} S_{1/(\beta+\beta_L)}(C_{Y_L}) V_{Y_L}^T \\ s.t.\ \ Y_L = \frac{\beta(U-S+Z/\beta)+\beta_L(X+Z_L/\beta_L)}{\beta+\beta_L}\end{aligned} \tag{14}$$

where $U_Y C V_Y^T = Y$ is the singular value decomposition of $Y$ and $C = diag(\sigma_1, \cdots \sigma_i, \cdots \sigma_n)$ is a diagonal matrix with all the singular values of $Y$ as diagonal elements. $S_\varepsilon(C)$ is the soft shrinkage of $C$, which is defined for every element of $C$ as $S_\varepsilon(\sigma) = \mathrm{sgn}(\sigma)\cdot\max(|\sigma|-\varepsilon, 0)$.

Similarly, the $S$ subproblem can be structured as

$$\min\quad \lambda\|S\|_1 + \frac{\beta}{2}\|S-(U-L+Z/\beta)\|_F^2 \tag{15}$$

Soft shrinkage [41] has been exploited to calculate the optimal solution of the sparse problem of L1 norm. The solution can be obtained in one step.

$$\begin{aligned}S = S_{\lambda/\beta}(Y_S) \\ s.t.\ \ Y_S = U - L + Z/\beta\end{aligned} \tag{16}$$

*2) U subproblem:* The $U$ subproblem is composed of two Frobenius-norm fidelity terms and an inner product term contains the Lagrange multiplier. Thus, the subproblem can be reformulated as:

$$\min\quad \frac{\mu}{2}\|HU-\Phi\|_F^2 + \frac{\beta}{2}\|U-(L+S+Z/\beta)\|_F^2 \tag{17}$$

This is a convex minimization problem and the solution can be expressed directly by:

$$U = \left(\mu H^T H + \beta\right)^{-1}[\mu H^T\Phi + \beta(L+S+Z/\beta)] \tag{18}$$

*3) X subproblem:* Extracting the $X$-related terms from eq. (11) and providing the appropriate constants to formulate the $X$ subproblem as:

$$\min\ \gamma\|DX\|_1 + \frac{\beta_L}{2}\|X-Q\|_F^2 \quad s.t.\ Q = L - Z_L/\beta_L \tag{19}$$

The minimization of the gradient-based L1 norm can be solved using the iterative method provided in [6]:

$$\begin{aligned}\left[I^T I + \frac{2\gamma}{\beta_L}\left(D^T W^{X_t^k} D\right)\right] X_t^{k+1} = Q_t \\ s.t.\ \ W^{X_t^k} = 1/2 diag[1/\sqrt{\left|\left[DX_t^k\right]_i\right|^2+\alpha}]\end{aligned} \tag{20}$$

where $I$ is the identity matrix. The subscript $t$ of the matrix $Q$ represents the $t$-th column of $Q$. $X_t^k$ represents the $t$-th column of the matrix $X$ at the $k$-th iteration, and $W^{X_t^k}$ is the corresponding weight matrix defined with a microscale $\alpha \to 0$.

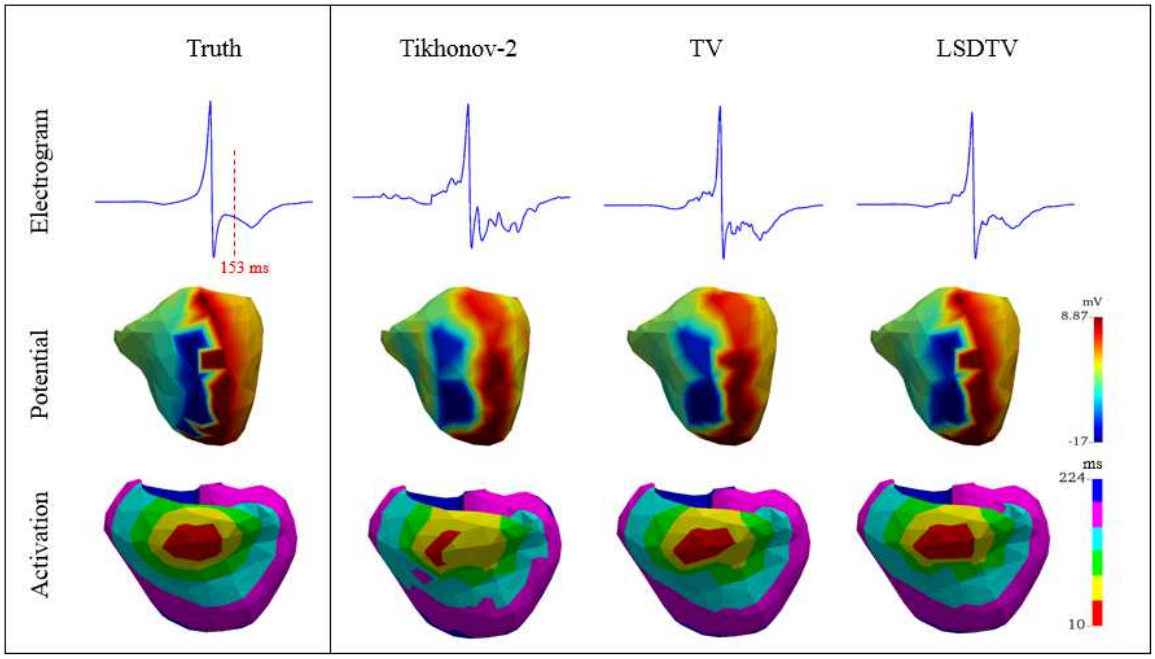


Fig. 3: Comparison between the true value and the reconstruction of the cardiac electrograms, heart-surface potentials, and activation maps. The experiment was based on a simulated single pacing of the RV-anterior.The first line displays the cardiac electrogram on a mesh node (Number: 455, on LV-endocardium) of the ventricular model.The second line displays the spatial distribution of EEP at a moment (153ms, depicted by a vertical line in the fist row) of the pacing rhythm. The third line displays the activation sequence.

**Algorithm 1** LSDTV Algorithm

**Require:** BSP matrix $\mathbf{\Phi}$, transfer matrix $H$, weighting coefficients $\lambda$, $\beta$, $\gamma$, $\mu$

1: **Initialize:** $U^0 = (H^T H + \lambda_0 I^T I)^{-1} H^T \mathbf{\Phi}$, $L^0 = S^0 = X^0 = 0$, $Z^0 = Z_L^0 = 0$
2: **repeat**
3: Update $L^{k+1}$ by eq. (14)
4: Update $S^{k+1}$ by eq. (16)
5: Update $U^{k+1}$ by eq. (18)
6: Update $X^{k+1}$ by eq. (20)
7: **until** $L$, $S$, $U$ are all converged

**Ensure:** $L$, $S$, $U$

### *D. Algorithm summary*

*1) Algorithm analysis:* As shown in Algorithm 1, the LSDTV scheme consists of the sub-problems of $L$, $S$, $U$ and $X$. Among them, the original NP-hard rank function $rank(L)$ is replaced by its convex approximation, the nuclear norm $\|L\|_*$; and the sparse problem $\|S\|_0$ is also convexly relaxed by the L1 norm $\|S\|_1$. Thus, all sub-problems of LSDTV are minimizing convex problems. Under this premise, the optimal solution is obtained by alternating iterative updates of the ADMM algorithm, which is proved to have objective convergence [42].

To overcome the mathematical ill-posedness of the inverse problem, the zero-order Tikhonov regularization is applied to initialize the EEP matrix before the first iteration:

$$U^0 = (H^T H + \lambda_0 I^T I)^{-1} H^T \mathbf{\Phi} \tag{21}$$

where $I$ is the identity matrix. In the case where the number of body-surface electrodes is much smaller than the number of cardiac mesh nodes, the time complexity of the initialization is $O(m^3)$. In each iteration, the $L$, $S$, and $U$ problems can be directly solved by one-step calculation, and their time complexity is $O(m^2 n + n^2 m)$, $O(nm)$, and $O(m^3 + m^2 n)$, respectively. The $X$ problem, that is, the procedure to solve the TV problem is completed by iteration, and the time complexity of a single step is $O(m^2 n^2)$, where $L, S, U, X, Z \in R^{m \times n}$. The overall time consumed by the LSDTV algorithm in the experiments is listed in Table V and discussed in section IV-C.

*2) Parameter description:* In the initialization of eq. (21), the setting of the balance parameter $\lambda_0$ of Tikhonov-0 has been discussed in many literatures [22], [43]. In this study, the L-curve [22] method was used to determine the value of $\lambda_0$. In the optimization process, scalars $\lambda, \gamma, \mu, \beta, \beta_L$ were used to balance the minimization target. Among them, $\lambda$ was used to balance the low-rank constraint with the sparse constraint, where $1/\sqrt{\max(m,n)}$ was considered to be an appropriate choice for $\lambda$ [41], $S \in R^{m \times n}$. Parameter $\gamma$ controlled the tradeoff between the nuclear and the TV norm to find a balance between the low-rank and smoothness of the potential background. $\mu$ is the weighting parameter of the fidelity term, which plays a role in balancing the estimated value in accordance with the priori conditions and the body-surface recordings. In this study, $\gamma$ was empirically set to 0.1, and $\mu$ lied in [0.01, 0.1]. The experimental performance of $\gamma$ and $\mu$ is discussed in section IV-B. $\beta, \beta_L$ are Lagrangian penalty parameters, which are fixed to 0.1 in this study, referring to the previous work [36].

TABLE I: Localization errors of the simulated 8 pacing sites.

| Pacing site | TV | LSDTV |
|---|---|---|
| **LV** | **localization error (mm)** | |
| anterior | 28.34 | 10.13 |
| apex | 8.92 | 2.51 |
| lateral-endo | 7.81 | 4.32 |
| lateral-epi | 4.84 | 1.40 |
| lateral | 11.36 | 9.20 |
| septum | 29.45 | 15.64 |
| **RV** | | |
| anterior | 14.05 | 3.36 |
| posterior | 24.82 | 13.10 |

TABLE II: Mean and standard deviation of location errors of ventricular pacing sites on subject 1.

| Pacing site | | TV | | LSDTV | |
|---|---|---|---|---|---|
| **LV** | **beats** | **mean(mm)** | **std(mm)** | **mean(mm)** | **std(mm)** |
| 1 | 28 | 27 | 8 | **14** | **7** |
| 2 | 33 | 20 | 8 | **10** | **8** |
| 3 | 29 | 25 | 8 | **15** | **9** |
| 4 | 33 | 20 | 6 | **8** | **4** |
| 5 | 34 | 23 | 3 | **13** | **5** |
| 6 | 34 | 23 | 5 | **11** | **8** |
| 7 | 34 | 21 | 3 | **11** | **5** |
| 8 | 21 | 22 | 6 | **13** | **5** |
| 9 | 20 | 24 | 3 | **14** | **5** |
| 10 | 28 | 25 | 9 | **12** | **9** |
| 11 | 33 | 24 | 6 | **12** | **6** |
| 12 | 31 | 23 | 12 | **12** | **5** |
| 13 | 24 | 22 | 5 | **8** | **4** |
| 14 | 25 | 25 | 8 | **12** | **5** |
| 15 | 21 | 18 | 8 | **6** | **6** |
| 16 | 17 | 20 | 5 | **9** | **5** |
| 17 | 22 | 25 | 5 | **13** | **3** |
| **RV** | **beats** | **mean(mm)** | **std(mm)** | **mean(mm)** | **std(mm)** |
| 1 | 28 | 19 | 7 | **8** | **4** |
| 2 | 24 | 28 | 6 | **11** | **1** |
| 3 | 25 | 25 | 9 | **13** | **8** |
| 4 | 25 | 24 | 4 | **12** | **4** |
| 5 | 25 | 21 | 6 | **9** | **5** |

TABLE III: Mean and standard deviation of location errors of ventricular pacing sites on subject 2.

| Pacing site | | TV | | LSDTV | |
|---|---|---|---|---|---|
| **LV** | **beats** | **mean(mm)** | **std(mm)** | **mean(mm)** | **std(mm)** |
| 1 | 32 | 19 | 2 | **11** | **4** |
| 2 | 34 | 27 | 6 | **16** | **6** |
| 3 | 15 | 23 | 5 | **12** | **6** |
| 4 | 31 | 24 | 6 | **15** | **7** |
| 5 | 33 | 22 | 4 | **14** | **5** |
| 6 | 34 | 20 | 4 | **12** | **7** |
| 7 | 23 | 18 | 4 | **10** | **4** |
| 8 | 34 | 19 | 4 | **12** | **5** |
| 9 | 37 | 20 | 2 | **10** | **3** |
| 10 | 37 | 23 | 4 | **14** | **4** |
| 11 | 11 | 22 | 5 | **14** | **8** |
| 12 | 34 | 21 | 4 | **12** | **4** |
| 13 | 15 | 19 | 5 | **8** | **5** |
| **RV** | **beats** | **mean(mm)** | **std(mm)** | **mean(mm)** | **std(mm)** |
| 1 | 22 | 19 | 3 | **9** | **2** |
| 2 | 34 | 25 | 8 | **15** | **8** |
| 3 | 35 | 19 | 5 | **9** | **3** |
| 4 | 39 | 19 | 6 | **11** | **7** |
| 5 | 12 | 20 | 3 | **10** | **1** |
| 6 | 17 | 32 | 3 | **23** | **4** |
| 7 | 38 | 24 | 3 | **12** | **3** |
| 8 | 22 | 20 | 5 | **12** | **5** |

## III. EXPERIMENTS

In this section, we evaluate the proposed algorithm through a series of experiments on locating the origin of ventricular pacing from the simulated ventricular pacing data with 8 different pacing sites, real intervention pacing data with 43 different pacing sites, and the data from 11 cases of clinical PVC patients. The results of the proposed LSDTV algorithm have been compared with the quadratic method Tikhonov-2 [19], and the non-quadratic method TV [6].

### *A. Simulation Experiments*

We evaluated the accuracy of the proposed algorithm for reconstructing EEP through a set of simulated data that included pacing in 8 different locations on the left ventricle (LV) and the right ventricle (RV). Data were provided by Karlsruhe Institute of Technology (KIT) [44] and shared on the Internet database - Experimental Data and Geometric Analysis Repository (EDGAR [45], http://edgar.sci.utah.edu/). Three quantities, endocardial and epicardial potential, activation time, and cardiac electrograms, were reconstructed in this experiment. Among them, the activation time was defined when the negative derivative ($-du_t/dt$) of the electrogram reached a maximum. To quantitatively analyze the accuracy of reconstruction, the relative errors (RE) and correlation coefficient (CC) between the reconstructed quantities and the ground truth, were utilized as: RE $= \sqrt{\frac{\sum_{i=1}^{m}(x_{r_i}-x_{t_i})^2}{\sum_{i=1}^{m}(x_{t_i})^2}}$, CC $= \frac{Cov(x_r,x_t)}{\sqrt{V(x_r)}\sqrt{V(x_t)}}$, where $x_r$ is a column vector of the reconstructed quantity and $x_t$ is the corresponding ground truth; $m$ is the number of mesh nodes of the heart surface; $Cov(x_r, x_t)$ is the covariance between the reconstructed quantity and the ground truth and $V(\cdot)$ represents variance.

Fig. 2 shows the mean and standard deviation of the CC and RE of the EEP for the ventricular pacing cases at 8 different pacing sites during the pacing rhythm, which is decomposed into 200-300 time nodes. Here, CC and RE represent the similarity between the spatial distribution of the reconstructed value and the true value of each frame EEP. As shown in Fig. 2, the CC of the LSDTV result is higher than that of the TV and Tikhonov-2, and the RE is lower than that of the TV and Tikhonov-2, indicating that the spatial fidelity of the LSDTV is better. Moreover, from the standard deviation of the CC statistical results, the standard deviation of the LSDTV is significantly lower compared with that provided by TV and Tikhonov-2. Hence, the reconstruction quality of different frames is relatively stable during the pacing rhythm. This is in line with expectations, because the low-rank and sparse constraints in the proposed LSDTV algorithm are macroscopic constraints, which are applied to the spatiotemporal EEP matrix of the pacing dynamic. Therefore, the proposed method can reconstruct a more accurate EEP spatiotemporal distribution. More specific reconstruction results are shown in Fig. 3.

Fig. 3 provides an example of ventricular pacing on the RV-anterior, showing three reconstructed quantities: the EEP

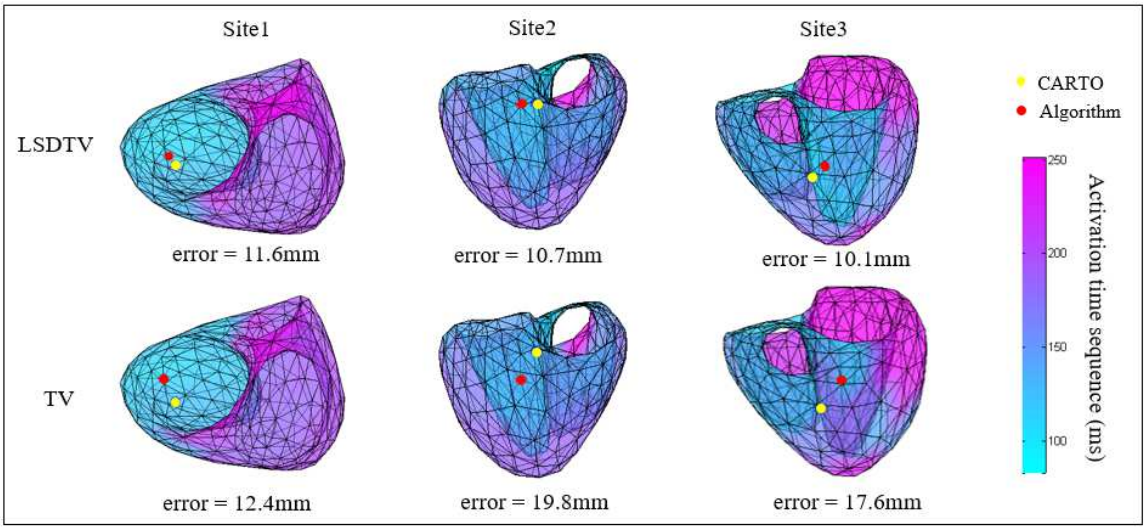


Fig. 4: Comparison between the deviation of the pacing sites obtained by the CARTO system, TV, and LSDTV. The color bar from blue to purple indicates activation time from early to late. The yellow dots mark the ventricular pacemaker points recorded by the CARTO system, and the red ones mark the ventricular pacemaker points calculated by the reconstruction algorithm LSDTV (top row) and TV (bottom row). The deviation distance between the three-dimensional coordinates of the pacing points recorded by CARTO and that reconstructed by the algorithm is shown below each ventricle geometry model.

spatial distribution at a given moment, the electrogram of a pacing period at a heart-mesh node, and the ventricular activation map. The top row in Fig. 3 shows the true electrogram of a mesh node during the pacing rhythm and the electrograms reconstructed by the Tikhonov-2, TV, and LSDTV methods. Because the first two methods are both based on spatial smoothing solutions of EEP, there are no constraints on their temporal continuity. Therefore, a certain level of noise arises in the electrograms over time, and the patterns become somewhat distorted. The LSDTV method is based on the spatiotemporal characteristics of the dynamic EEP and can provide a relatively stable electrogram (CC=0.99, RE=0.14), compared with Tikhonov-2 (CC=0.93, RE=0.42) and TV (CC=0.96, RE=0.33). The middle row of Fig. 3 shows the spatial distribution of EEP at an instant in the propagation of the electrical excitement. As shown, Tikhonov-2 provides an overly smooth solution (CC=0.61, RE=0.71). The TV method (CC=0.70, RE=0.60) maintains a steep gradient between the high and low potentials, but with some compromises in potential details, such as corner details of positive and negative potential shapes. The proposed LSDTV method (CC=0.77, RE=0.48) provides accurate spatial distribution of EEP with complete details. The bottom row of Fig. 3 illustrates the real value of the activation map and the solutions of Tikhonov-2, TV, and LSDTV. The color bar, which ranges from red to blue, indicates the activation from earlier to later. As shown, the earliest activation is located at the anterior RV. As a result, LSDTV (CC=0.84, RE=0.17) provides a more realistic activation time compared with the Tikhonov-2 (CC=0.71, RE=0.25) and TV (CC=0.77, RE=0.21) methods. Table I lists the localization errors of the 8 simulated pacing sites by TV and LSDTV. As shown, LSDTV provides a more accurate localization, benefiting from its use of spatiotemporal correlation information.

### *B. Real Ventricular Pacing Experiments*

The proposed algorithm was validated by experimenting with two types of real ventricular pacing datasets. The first type is intervention pace, containing body surface recordings of 1183 heart beats of 43 different pacing sites from 2 healthy hearts being paced with a catheter device, and the (x, y, z) locations of the pacing sites are recorded in the CARTO system. This dataset was also obtained from EDGAR [45], which has been presented in some other publications such as [34]. We evaluated the accuracy of the algorithm by comparing the three-dimensional coordinates of the reconstructed pacing sites and those recorded by the CARTO system. The other type of data was obtained from ablation surgeries of 11 patients with real PVC, including synchronized body-surface potential recordings and activation maps reconstructed by the Ensite system. The contributors to the data are researchers at the Zhejiang Provincial Hospital. We compared the premature beat positions obtained by the Ensite reconstruction and the algorithm reconstruction to judge the correctness of the algorithm.

*1) Intervention pace:* In this part, the pacing was done on the cardiac surface of the left/right ventricles of the two subjects. Fig. 4 shows an example of three pacing sites for subject 1 to demonstrate their activation maps and pace origins reconstructed by the LSDTV and TV algorithm respectively. The yellow dots mark the (x, y, z) locations of the pacing sites recorded in the CARTO system, which is used as the gold standard in this experiment. As shown, the deviation of the pacing sites calculated by the LSDTV algorithm from the gold standard is approximately 10 mm, which is more accurate than the TV algorithm alone. This is consistent with the expectation, because it can be seen from the simulation experiment results in Fig. 3 that LSDTV can reconstruct a more stable electrogram, which is beneficial for calculating

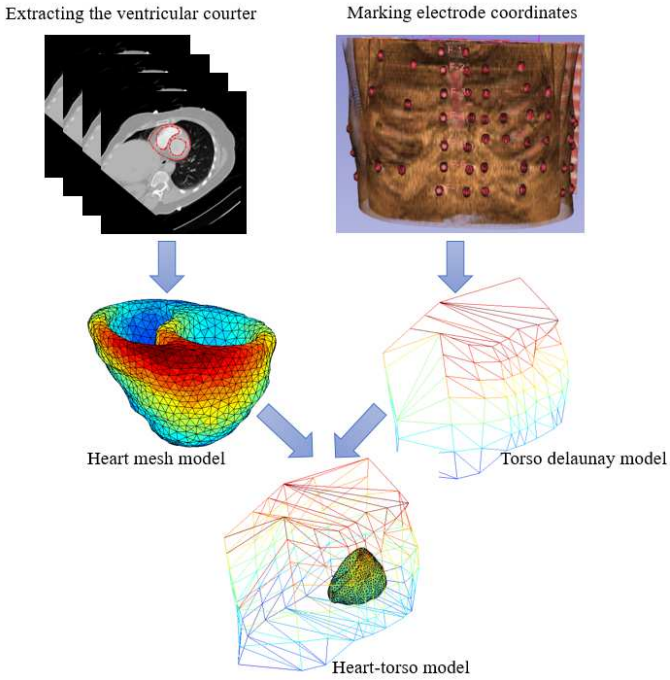


Fig. 5: Process of creating a heart-torso geometric model. The torso geometry model (determined by the body-surface electrodes) and the ventricular surface model are derived from CT data.

the activation time, so that the earliest activation point can be judged more accurately.

Tables II and III summarize the mean and standard deviation of the positioning error of the pacing sites for subject 1 and subject 2. The number of beats at each pacing site is shown in the second column of the tables, and a pacing site coordinate is estimated for each beat. It can be seen from the statistical results that the deviation distance between the pacemaker point reconstructed from LSDTV and the gold standard is approximately 10 mm, which is significantly reduced compared with the error of approximately 20 mm for TV reconstruction. This is consistent with our analysis above.

*2) Clinical PVC:* In this part, we validated the effectiveness of the proposed LSDTV method in clinical diagnosis for 11 real patients with PVC. The patients were consented for the following diagnosis, and it was performed according to a protocol approved by the ethical committee of Zhejiang Provincial Hospital. The subjects' heart-torso geometric models were taken from the thoracic CT scan with a spatial resolution of axial 0.6-1 mm. As shown in Fig. 5, the 3D heart model was constructed from the outline of the heart surface (including the endocardium and epicardium) extracted from the CT slices. The torso model was created by matching the 64-electrode positions to a standard torso template with 235 triangles of Delaunay triangulation. Then, the forward model was solved as mentioned in section II-A. In addition, the body-surface potentials were recorded as the 64-electrode ECGs, sampled at 2 kHz, which were recorded simultaneously with the invasive electrophysiological data (gold standard) from the Ensite3000 system.

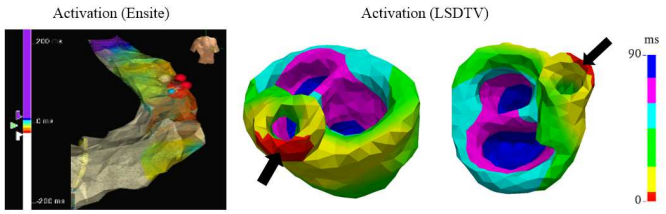


Fig. 6: Activation maps of ventricular premature beat in the anterior RVOT reconstructed by the Ensite3000 system and the proposed LSDTV method.

Fig. 6 shows the diagnosis of a 58-year-old PVC subject. On the left side, the 3D model of the right ventricle outflow tract (RVOT) and the activation map, which was reconstructed invasively by the Ensite3000 system during catheter ablation, are shown. The red globules mark the ablation target, which is the ectopic pacing site that is located at the anterior RVOT. The activation maps of the two perspectives were derived from EEPs, reconstructed by the LSDTV method and shown on the right side of Fig. 6. The red site, distinguished by the black arrow, is the earliest activation, located at the anterior RVOT (the funnel-shaped outlet above the right ventricle), consistent with the result of invasive measurement.

In addition, a total of 10 symptomatic patients with ectopic ventricular pacing were enrolled. The basic information of the subjects, including diagnosis of disease, the ectopic pacing sites located by the intraoperative diagnosis, and the results calculated by the LSDTV algorithm are listed in Table IV. For the 10 PVCs provided in the table, the proposed method can correctly point out the position of the ectopic pacemaker. Note: The 3D ventricular model in this study does not contain a pulmonary valve and therefore does not study the relative position of the ectopic precordial point and the pulmonary valve as diagnosed by the Ensite system in case 4 and case 6.

## IV. Discussion

### A. Robustness to initializations

The LSDTV algorithm proposed in this paper was used to estimate the optimal solution in the inverse problem of cardiac electrophysiology. A suitable initialization method is needed to overcome the mathematical underdetermination caused by low-dimensional body surface measurements. This is because the effectiveness of the low-rank, sparse, and gradient sparse (TV) constraints in the LSDTV algorithm is to trim the rough initialization results toward the real situation. The best initial input of the algorithm to overcome the mathematical underdetermination problem must be fuzzy, so as to ensure that the cardiac potential is completely reconstructed without loss. In this study, Tikhonov-0 was employed to provide initial input for the algorithm. To discuss the robustness of LSDTV with different initial inputs, here we compare the performance of LSDTV under initializations of the different-order Tikhonov. Fig. 7 shows the simulation results of eight different pacing positions using the initial input calculated by Tikhonov-0, Tikhonov-1, and Tikhonov-2. As shown, the Tikhonov initialization of different orders does not make a

TABLE IV: Diagnosis information for 10 patients with PVC: age, sex, diagnostic, and the origin of ectopic pacing located by the Ensite system and proposed LSDTV algorithm.

| No. | Age | Sex | Rate | Diagnosis | Imaging modality | Location (Ensite3000) | | Location (LSDTV) | |
|---|---|---|---|---|---|---|---|---|---|
| | | | | | | Ventricle | Site | Ventricle | Site |
| 1 | 52 | male | frequent | PVC | CT | LV | Apical free wall | LV | Apical free wall |
| 2 | 64 | female | frequent | PVC | CT | RV | Near the ventricle septum | RV | Near the ventricle septum |
| 3 | 47 | female | frequent | PVC | CT | RV | Posterior RVOT | RV | Posterior RVOT |
| 4 | 45 | female | frequent | PVC & Anemia | CT | RV | Posterior RVOT under pulmonary valve | RV | Posterior RVOT |
| 5 | 57 | female | frequent | PVC | CT | RV | Anterior RVOT | RV | Anterior RVOT |
| 6 | 58 | female | occasional | PVC & Hypertension | CT | RV | Anterior RVOT under pulmonary valve | RV | Anterior RVOT |
| 7 | 53 | female | frequent | PVC | CT | RV | Free wall of RVOT | RV | Free wall of RVOT |
| 8 | 33 | male | frequent | PVC | CT | RV | Posterior RVOT | RV | Posterior RVOT |
| 9 | 58 | female | frequent | PVC & Cerebral infarction sequelae | CT | RV | Posterior RVOT | RV | Posterior RVOT |
| 10 | 34 | male | frequent | PVC | CT | RV | Posterior RVOT | RV | Posterior RVOT |

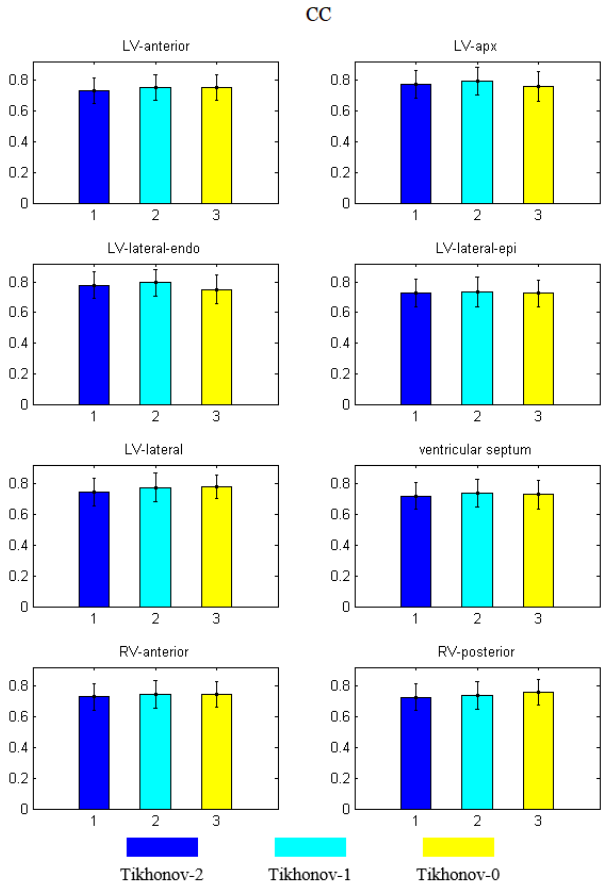


Fig. 7: CC statistics of the inversion results of 8 pacing sites based on Tikhonov of different orders as the initialization method. The color histograms represent the CC average of all frames of the pacing period. Error bar shows the standard deviation of results.

significant difference to the CC of the result. The proposed algorithm is robust to the required initialization values.

### B. Parameter analysis

In Section II-D, we briefly summarized the setting of the balance parameters in the LSDTV algorithm. Among them, the weighting factor $\gamma$ for TV item and balance parameter $\mu$ for the fidelity term were selected empirically. Therefore, the experimental performance of these two parameters is demonstrated in Fig. 8.

In this part, the simulated LV-apex pacing experiment was taken as an example to explore the sensitivity of the solution to the parameters $\gamma$ and $\mu$. Here, the average CC and RE of all-time nodes during the pacing rhythm were used as criteria for reconstruction accuracy. Fig. 8(a) shows the trend of CC and RE for parameter $\gamma$ over the interval 0 to 1, when $\mu$ is fixed at 0.05. As shown, the closer $\gamma$ is to 0, the more sensitive the solution is to the change of the $\gamma$ and tends to be stable when $\gamma$ is close to 0.1. Overall, the solution is relatively insensitive to $\gamma$; therefore, $\gamma$ is fixed at 0.1 in this study. On the other hand, the parameter $\mu$ represents the ability to constrain the consistency of the solution with the measured data during the optimization process. As shown in Fig. 8(b), when $\mu$ approaches 0, the accuracy of the reconstruction is low and oscillating because the solution deviates significantly from the body-surface recording. A relatively stable and accurate solution can be obtained when $\mu$ is in the interval of [0.01, 0.1]. Thus, in the experiments of this study, $\mu$ lied in [0.01, 0.1].

### C. Strengths and weaknesses

This study proposes a new framework combining LSD and TV to solve the inverse problem of ECG imaging to accurately locate the origin of PVC. For the first time, LSD decomposition applies the concept of decomposing potential background and foreground for reconstruction of ECG imaging. $S$ matrix plays an effective role in protecting the sparse potential detail in reconstruction. In addition, the sparsity of the $S$ matrix also filters the noise to some extent. The TV-constrained low-rank matrix $L$ forces a smooth and low-level potential background, which explains the remainder of the potential removal from the high/low potential spikes. TV is edge-preserving smooth constraints, and there is a certain degree of compromise in the potential details. Therefore, in this study, TV only acts on the potential background to filter Gaussian noise but avoids compromise of potential details.

Although the LSDTV method improves the accuracy of potential reconstruction, there are some weaknesses. From the point of view of PVC localization, the potential-based method is not as direct as the activation-based imaging method, lacking the physiological significance of direct usage, and further derivation of activation time is needed. In terms of computational cost, LSDTV inevitably requires a large number

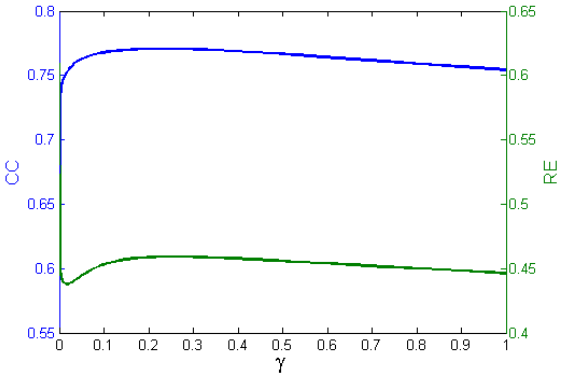


(a)

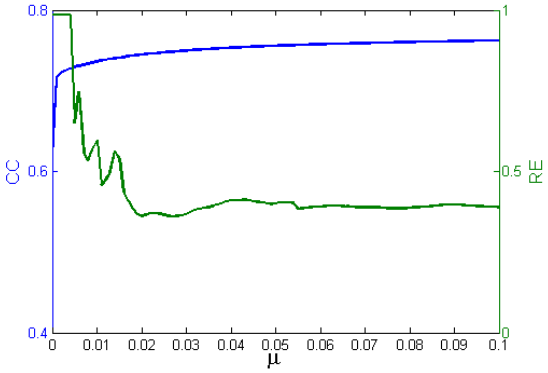


(b)

Fig. 8: Sensitivity of the solution to the $\gamma$ and $\mu$ parameters.

TABLE V: Comparison of computing time between LSDTV and TV.

| site | frames | computing time (ms) | |
|---|---|---|---|
| | | TV | LSDTV |
| LV-apex | 230 | 701 | 1426 |
| LV-lateral | 266 | 712 | 1451 |
| RV-posterior | 225 | 677 | 1373 |

of singular value decomposition calculations, which increases the calculation time. Table V lists the calculation times of the three cases of simulated ventricular pacing experiments. It can be seen that the calculation time of the LSDTV method is approximately twice as that of the conventional TV. The computation of experiments in our study was processed by MATLAB R2014a with a 3.4 GHz processor and 8 GB RAM.

The abovementioned deficiencies help us clear the direction of future efforts as follows: 1) Optimize the potential-to-activation transformation method to improve the accuracy of activation imaging; 2) Optimize the calculation process of LSDTV to reduce the computation time and memory loss.

## V. Conclusion

In this paper, an LSDTV framework based on low-rank sparse decomposition + TV constraints is proposed to solve the ill-posed problem of dynamic EEP reconstruction. This method utilizes the spatiotemporal correlation of potential dynamics to improve the accuracy of the inverse solution. The LSDTV method has been shown to accurately reconstruct the EEP distribution and correctly reveal the origin of the pacing rhythm in simulated ventricular pacing, real intervention pacing, and clinical PVC experiments.

## References

[1] E. Hoffmann, P. Nimmermann, C. Reithmann, F. Elser, T. Remp, and G. Steinbeck, "New mapping technology for atrial tachycardias," *Journal of Interventional Cardiac Electrophysiology*, vol. 4, no. 1, pp. 117–120, 2000.

[2] T. Paul, B. Windhagenmahnert, T. Kriebel, H. Bertram, R. Kaulitz, T. Korte, M. Niehaus, and J. Tebbenjohanns, "Atrial reentrant tachycardia after surgery for congenital heart disease endocardial mapping and radiofrequency catheter ablation using a novel, noncontact mapping system," *Circulation*, vol. 103, no. 18, p. 2266, 2001.

[3] M. Dubuc, R. Nadeau, G. Tremblay, T. Kus, F. Molin, and P. Savard, "Pace mapping using body surface potential maps to guide catheter ablation of accessory pathways in patients with wolff-parkinson-white syndrome," *Circulation*, vol. 87, no. 1, p. 135, 1993.

[4] G. Li and B. He, "Localization of the site of origin of cardiac activation by means of a heart-model-based electrocardiographic imaging approach," *IEEE Transactions on Biomedical Engineering*, vol. 48, no. 6, pp. 660–669, 2001.

[5] Z. Liu, C. Liu, and B. He, "Noninvasive reconstruction of three-dimensional ventricular activation sequence from the inverse solution of distributed equivalent current density," *IEEE Transactions on Medical Imaging*, vol. 25, no. 10, pp. 1307–1318, 2006.

[6] S. Ghosh and Y. Rudy, "Application of l1-norm regularization to epicardial potential solution of the inverse electrocardiography problem," *Annals of Biomedical Engineering*, vol. 37, no. 5, pp. 902–912, 2009.

[7] B. He, G. Li, and X. Zhang, "Noninvasive imaging of cardiac transmembrane potentials within three-dimensional myocardium by means of a realistic geometry anisotropic heart model," *IEEE Transactions on Biomedical Engineering*, vol. 50, no. 10, pp. 1190–1202, 2003.

[8] P. M. van Dam, T. F. Oostendorp, and A. van Oosterom, "Application of the fastest route algorithm in the interactive simulation of the effect of local ischemia on the ecg," *Medical & biological engineering & computing*, vol. 47, no. 1, pp. 11–20, 2009.

[9] B. Tilg, G. Fischer, R. Modre, F. Hanser, B. Messnarz, M. Schocke, C. Kremser, T. Berger, F. Hintringer, and F. X. Roithinger, "Model-based imaging of cardiac electrical excitation in humans." *IEEE Transactions on Medical Imaging*, vol. 21, no. 9, p. 1031, 2002.

[10] B. He, G. Li, and X. Zhang, "Noninvasive three-dimensional activation time imaging of ventricular excitation by means of a heart-excitation model." *Physics in Medicine & Biology*, vol. 47, no. 22, pp. 4063–4078, 2002.

[11] L. Yu, Q. Jin, Z. Zhou, L. Wu, and B. He, "Three-dimensional noninvasive imaging of ventricular arrhythmias in patients with premature ventricular contractions," *IEEE Transactions on Biomedical Engineering*, vol. 65, no. 7, pp. 1495–1503, 2018.

[12] L. Wang, O. A. Gharbia, S. Nazarian, B. M. Horáček, and J. L. Sapp, "Non-invasive epicardial and endocardial electrocardiographic imaging for scar-related ventricular tachycardia," *EP Europace*, vol. 20, no. FI2, pp. f263–f272, 2018.

[13] W. H. Schulze, Z. Chen, J. Relan, D. Potyagaylo, M. W. Krueger, R. Karim, M. Sohal, A. Shetty, Y. Ma, N. Ayache *et al.*, "Ecg imaging of ventricular tachycardia: evaluation against simultaneous non-contact mapping and cmr-derived grey zone," *Medical & biological engineering & computing*, vol. 55, no. 6, pp. 979–990, 2017.

[14] P. M. van Dam, R. Tung, K. Shivkumar, and M. Laks, "Quantitative localization of premature ventricular contractions using myocardial activation ecgi from the standard 12-lead electrocardiogram," *Journal of Electrocardiology*, vol. 46, no. 6, pp. 574–579, 2013.

[15] G. Fischer, B. Tilg, P. Wach, G. Lafer, and W. Rucker, "Analytical validation of the bemapplication of the bem to the electrocardiographic forward and inverse problem," *Computer Methods and Programs in Biomedicine*, vol. 55, no. 2, pp. 99–106, 1998.

[16] M. Potse, B. Dubé, and A. Vinet, "Cardiac anisotropy in boundary-element models for the electrocardiogram," *Medical & Biological Engineering & Computing*, vol. 47, no. 7, pp. 719–729, Jul 2009. [Online]. Available: https://doi.org/10.1007/s11517-009-0472-x

[17] G. Seemann, D. U. Keller, M. W. Krüger, F. M. Weber, M. Wilhelms, and O. Dössel, "Electrophysiological modeling for cardiology: methods and potential applications," *it-Information Technology Methoden und innovative Anwendungen der Informatik und Informationstechnik*, vol. 52, no. 5, pp. 242–249, 2010.

[18] G. Fischer, B. Tilg, R. Modre, and F. Hanser, "On modeling the wilson terminal in the boundary and finite element method," *IEEE Transactions on Biomedical Engineering*, vol. 49, no. 3, pp. 217–224, 2002.

[19] D. Calvetti and L. Reichel, "Tikhonov regularization of large linear problems," *BIT Numerical Mathematics*, vol. 43, no. 2, pp. 263–283, 2003.

[20] P. R. Johnston and R. M. Gulrajani, "Selecting the corner in the l-curve approach to tikhonov regularization," *IEEE Transactions on Biomedical Engineering*, vol. 47, no. 9, pp. 1293–1296, 2000.

[21] A. N. Tikhonov and V. Y. Arsenin, "Solutions of ill-posed problems," *Mathematics of Computation*, vol. 32, no. 144, pp. 491–491, 1977.

[22] P. C. Hansen and D. P. O"Leary, "The use of the l-curve in the regularization of discrete ill-posed problems," *Siam J.sci.comput*, vol. 14, no. 6, pp. 1487–1503, 1993.

[23] P. R. Johnston and R. M. Gulrajani, "A new method for regularization parameter determination in the inverse problem of electrocardiography," *IEEE Transactions on Biomedical Engineering*, vol. 44, no. 1, p. 19, 1997.

[24] Y. Okamoto, Y. Teramachi, and T. Musha, "Limitation of the inverse problem in body surface potential mapping," *IEEE Transactions on Biomedical Engineering*, vol. BME-30, no. 11, pp. 749–754, 2007.

[25] B. W. Rust and B. W. Rust, *Truncating the singular value decomposition for ill-posed problems*. US Department of Commerce, Technology Administration, National Institute of Standards and Technology, 1998.

[26] B. Messnarz, B. Tilg, R. Modre, G. Fischer, and F. Hanser, "A new spatiotemporal regularization approach for reconstruction of cardiac transmembrane potential patterns," *IEEE Transactions on Biomedical Engineering*, vol. 51, no. 2, pp. 273–281, 2004.

[27] G. Shou, L. Xia, M. Jiang, Q. Wei, F. Liu, and S. Crozier, "Truncated total least squares: a new regularization method for the solution of ECG inverse problems," *IEEE Transactions on Biomedical Engineering*, vol. 55, no. 4, pp. 1327–1335, 2008.

[28] M. Jiang, L. Xia, G. Shou, and M. Tang, "Combination of the LSQR method and a genetic algorithm for solving the electrocardiography inverse problem." *Physics in Medicine & Biology*, vol. 52, no. 5, pp. 1277–94, 2007.

[29] T. S. Ruud, B. F. Nielsen, M. Lysaker, and J. Sundnes, "A computationally efficient method for determining the size and location of myocardial ischemia," *IEEE Transactions on Biomedical Engineering*, vol. 56, no. 2, pp. 263–272, 2009.

[30] Y. Serinagaoglu, D. H. Brooks, and R. S. Macleod, "Improved performance of bayesian solutions for inverse electrocardiography using multiple information sources," *IEEE Transactions on Biomedical Engineering*, vol. 53, no. 10, pp. 2024–2034, 2006.

[31] L. Wang, J. Qin, T. T. Wong, and P. A. Heng, "Application of l1-norm regularization to epicardial potential reconstruction based on gradient projection." *Physics in Medicine & Biology*, vol. 56, no. 19, pp. 6291–6310, 2011.

[32] S. Twomey, "On the numerical solution of fredholm integral equations of the first kind by the inversion of the linear system produced by quadrature," *Journal of the ACM (JACM)*, vol. 10, no. 1, pp. 97–101, 1963.

[33] Ü. Aydın and Y. Serinagaoglu, "Use of activation time based kalman filtering in inverse problem of electrocardiography," in *4th European Conference of the International Federation for Medical and Biological Engineering*. Springer, 2009, pp. 1200–1203.

[34] B. Erem, J. Coll-Font, R. M. Orellana, P. St'ovicek, and D. H. Brooks, "Using transmural regularization and dynamic modeling for noninvasive cardiac potential imaging of endocardial pacing with imprecise thoracic geometry," *IEEE transactions on medical imaging*, vol. 33, no. 3, pp. 726–738, 2014.

[35] A. Majumdar, R. K. Ward, and T. Aboulnasr, "Non-convex algorithm for sparse and low-rank recovery: application to dynamic mri reconstruction," *Magnetic Resonance Imaging*, vol. 31, no. 3, pp. 448–455, 2013.

[36] S. Chen, H. Liu, Z. Hu, H. Zhang, P. Shi, and Y. Chen, "Simultaneous reconstruction and segmentation of dynamic pet via low-rank and sparse matrix decomposition." *IEEE Transactions on Biomedical Engineering*, vol. 62, no. 7, pp. 1784–1795, 2015.

[37] S. Niu, G. Yu, J. Ma, and J. Wang, "Nonlocal low-rank and sparse matrix decomposition for spectral ct reconstruction," *Inverse Problems*, vol. 34, no. 2, 2017.

[38] M. Shakeri and H. Zhang, "Moving object detection in time-lapse or motion trigger image sequences using low-rank and invariant sparse decomposition," in *IEEE International Conference on Computer Vision*, 2017, pp. 5133–5141.

[39] J. Wang and B. Shim, "Exact recovery of sparse signals using orthogonal matching pursuit: How many iterations do we need?" *IEEE Trans. Signal Processing*, vol. 64, no. 16, pp. 4194–4202, 2016.

[40] J. Xu, A. R. Dehaghani, F. Gao, and L. Wang, "Noninvasive transmural electrophysiological imaging based on minimization of total-variation functional." *IEEE Transactions on Medical Imaging*, vol. 33, no. 9, pp. 1860–74, 2014.

[41] E. J. Candès, X. Li, Y. Ma, and J. Wright, "Robust principal component analysis?" *Journal of the ACM (JACM)*, vol. 58, no. 3, p. 11, 2011.

[42] S. Boyd, N. Parikh, E. Chu, B. Peleato, J. Eckstein *et al.*, "Distributed optimization and statistical learning via the alternating direction method of multipliers," *Foundations and Trends® in Machine learning*, vol. 3, no. 1, pp. 1–122, 2011.

[43] P. R. Johnston and R. M. Gulrajani, "A new method for regularization parameter determination in the inverse problem of electrocardiography," *IEEE Transactions on Biomedical Engineering*, vol. 44, no. 1, pp. 19–39, 1997.

[44] W. H. Schulze, D. Potyagaylo, R. Schimpf, T. Papavassiliu, E. Tulumen, B. Rudic *et al.*, "A simulation dataset for ecg imaging of paced beats with models for transmural, endo-and epicardial and pericardial source imaging," *Germany: Bad Herrenalb*, 2015.

[45] K. Aras, W. Good, J. Tate, B. Burton, D. Brooks, J. Collfont, O. Doessel, W. Schulze, D. Potyagaylo, and L. Wang, "Experimental data and geometric analysis repository - edgar," *Journal of Electrocardiology*, vol. 48, no. 6, pp. 975–981, 2015.